# Uncertainty quantification of free stream conditions in non-equilibrium flow over a double-cone

A. Perlini[1], D. Ninni[2], F. Bonelli[2] and G. Gori[1]
Corresponding author: alberto.perlini@polimi.it
[1] Department of Aerospace Science and Technology, Politecnico di Milano, Via La Masa 34, 20156, Milano, Italy
[2] Department of Mechanics, Mathematics and Management, Polytechnic University of Bari, Via Re David 200, Bari, Italy

**Abstract:** Aleatoric uncertainties are propagated through a computational model representative of a reference experiment in hypersonics for which observations are available. Namely, a hypersonic stream over an axisymmetric double-cone. The flow exhibits strong non-equilibrium thermochemical effects. The inflow uncertainty is characterized and propagated through a computational model of the experiment using standard Polynomial Chaos Expansions. Global sensitivity analysis is performed via Sobol's method. Eventually, the true experimental inflow conditions are inferred from available experimental observations.

*Keywords:* Uncertainty Quantification, Calibration, Computational Fluid Dynamics, Hypersonics.

## 1. Introduction

The accurate prediction of wall quantities in hypersonic flows is still a challenging task, especially in the presence of strong thermochemical nonequilibrium and shock-wave/boundary-layer interaction (SWBLI). Double-cone [1] and double-wedge [2] configurations are widely used as reference test cases because they reproduce separated hypersonic flows while retaining a relatively simple geometry. Among the available studies, the work of Nompelis and Candler [3] represents a key reference, as it provided a broad numerical assessment of double-cone experiments under different flow conditions. Their results showed that numerical simulations are not able to correclty predict the extent of the separation-region. The prediction mismatch does not appear to be fully explained by wall-catalysis assumptions or by more detailed thermochemical models, suggesting that the uncertainty inherent in inflow conditions may play a major role [1]. Indeed, recent state-to-state analyses of the nozzle expansion [1] that produces the inflow stream have shown that the computed thermochemical state can differ significantly from that obtained with classical multi-temperature models. Such differences can alter the subsequent SWBLI over the double cone and, consequently, the predicted separation pattern.

In this context, we propagate aleatoric uncertainty through a computational model of the double-cone configuration investigated by Nompelis and Candler [3], for which experimental observations are available and strong thermochemical nonequilibrium effects are expected. To achieve our goal, the experiment is reproduced numerically using an in-house Computational Fluid Dynamics (CFD) solver developed at Politecnico di Bari [4]. The inflow uncertainty is first characterized, and then sampled to generate a database. The set of CFD output realizations serves the building of standard Polynomial Chaos Expansions (PCE) to perform the Uncertainty Quantification (UQ) analysis, including global sensitivity analysis via Sobol's method. Taking advantage of the available observations, we also infer the most likely inflow conditions attained during the experiment.

The paper is structured as follows. Section 2 describes the computational model created to perform CFD simulations, including the numerical and thermophysical setting. Section 3 briefly recalls the mathematics underlying the UQ framework. Lastly, Sec.4 presents the analysis of the double-cone experiment.

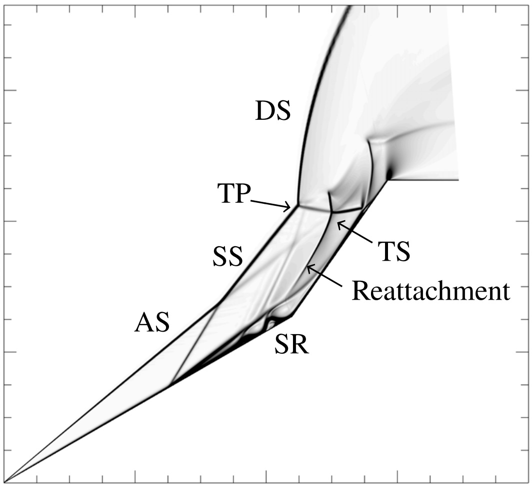


Figure 1: Numerically computed flow field structure over the double-cone.

## 2. Thermophysical modeling and numerical approach

The axisymmetric experiment is simulated by solving the Navier-Stokes equations for a neutral oxygen mixture. A generic flow field is reported in Fig. 1 to highlight the shock pattern. An attached shock (AS) forms at the first deflection. A detached curved shock (DS) is also well identified. As these two interact, two additional shocks appear: the transmitted shock (TS) i.e., the weakest one, and the separation shock (SS) responsible for the separation of the boundary layer (separation region, SR). The triple point (TP), where SS, DS, and TS coexist, identifies the location of the supersonic/subsonic transition.

Viscosities and binary mass-diffusion coefficients are obtained from Gupta's curve-fitted correlations [5]. The Eucken's relation computes thermal conductivities (translational and vibrational). Mixture-averaged properties are evaluated using standard mixing rules from [6, 7, 8]. Thermochemical nonequilibrium is modelled by the two-temperature approach, with kinetics data provided by Park [9]. Thermal nonequilibrium is accounted in dissociation/recombination processes of oxygen molecules, considering a geometric average of the roto-translational and vibrational temperatures. The latter is evaluated by considering a transport equation of the vibrational energy with Landau-Teller and preferential removal source terms.

The governing equations are discretized with a finite-volume solver on a structured body fitted mesh. An operator splitting approach is employed. First, a convective-diffusive (frozen) step solves the homogeneous Navier-Stokes equations. Then, the solution is updated integrating the thermo-chemical source terms. Convective fluxes are handled with the Steger and Warming flux vector splitting [10] with second-order accurate MUSCL (Monotonic Upstream-centered Scheme for Conservation Laws) reconstruction. Viscous terms are handled with the Gauss divergence theorem with linear interpolation. Time integration employs an explicit third-order accurate Runge-Kutta scheme [11]. The stiff chemical kinetics relies on an implicit Gauss-Seidel scheme. Further details can be found in [1, 4].

## 3. Uncertainty quantification framework

We employ a standard PCE to forward-propagate the uncertainty, see [12] and reduce the computational burden of the inferential procedure. We consider a generic output of the CFD model

$$Y = M(\boldsymbol{U}), \tag{1}$$

where $\boldsymbol{U}$ denotes a random input vector defined over the stochastic domain $\Omega \subseteq \mathbb{R}^d$, and $Y$ is the corresponding random output. The random input vector $\boldsymbol{U}$ parametrizes the uncertain test conditions. The computational model is assumed to be deterministic, such that each realization $\boldsymbol{u}$ of $\boldsymbol{U}$ uniquely determines a realization $y$ of $Y$. Furthermore, the uncertain inputs are assumed to be statistically independent, yielding the factorized joint probability density function

$$p_{\boldsymbol{U}}(\boldsymbol{u}) = \prod_{i}^{d} p_{U_i}(u_i). \tag{2}$$

Under this assumption, the stochastic response $Y$ can be mimicked through a PCE approximation $\hat{Y}$

$$\hat{Y} = M_{PC}(\boldsymbol{U}) = \sum_{\boldsymbol{\alpha} \in \mathcal{A}} c_{\boldsymbol{\alpha}} \Psi_{\boldsymbol{\alpha}}(\boldsymbol{U}), \tag{3}$$

where $\Psi_{\boldsymbol{\alpha}}(\boldsymbol{U})$ denotes a multivariate orthonormal polynomial basis indexed by the multi-index $\boldsymbol{\alpha}$ included in the set $\mathcal{A}$. Specifically, each component $\alpha_i$ identifies the degree of the univariate orthonormal polynomial $\psi_{\alpha_i}$ associated with the random variable $U_i$. In this work, we select the univariate polynomial of the Legendre family according to the Askey scheme [13]. The expansion is truncated at a maximum polynomial degree $r$, such that $\sum_i \alpha_i = r$ for all $\boldsymbol{\alpha} \in \mathcal{A}$. The theoretical convergence properties of PCE and the selection of the polynomial basis are extensively discussed in Refs. [12, 13].

The UQ analysis requires computing the expansion coefficients $c_{\boldsymbol{\alpha}}$ from available data (in our case CFD model realizations). The task is carried out using a least-square approach. Namely, let $\boldsymbol{\mathcal{U}} = \{\boldsymbol{u}^{(i)}, i = 1, \dots, n\}$ be the set of random training samples associated to $\boldsymbol{y} = \{y^{(1)} = M(\boldsymbol{u}^{(1)}), \dots, y^{(n)} = M(\boldsymbol{u}^{(n)})\}$ the vector of the corresponding model responses. Let $\boldsymbol{C} = \{C_{ij} = \Psi_j(\boldsymbol{u}^{(i)}),\ i = 1, \dots, n,\ j = 1, \dots, \operatorname{card} \mathcal{A}\}$ be the information matrix deriving from evaluating the polynomial basis at the inputs $\boldsymbol{\mathcal{U}}$. Then, the vector of coefficients comes from the solution of the following least-square minimization

$$\boldsymbol{c} = (\boldsymbol{C}^T \boldsymbol{C})^{-1} \boldsymbol{C}^T \boldsymbol{y}. \tag{4}$$

Once the coefficients are available, the QoI uncertainty can be efficiently characterized through a post-processing of the coefficients. Approximation of its mean $\mu_Y$ and variance $\sigma_Y^2$ is given by

$$\mu_Y = \mathbb{E}\left[Y\right] \approx c_{\boldsymbol{0}}, \qquad \sigma_Y^2 = \mathbb{E}\left[(Y - \mu_Y)^2\right] \approx \sum_{\substack{\boldsymbol{\alpha} \in \mathcal{A} \\ \boldsymbol{\alpha} \neq \boldsymbol{0}}} c_{\boldsymbol{\alpha}}^2. \tag{5}$$

Notoriously, algebraic manipulation of the coefficients return the Sobol' sensitivity indices [14].

Although we deal with spatially-dependent Quantities of Interest (QoIs), we build local PCE. While straightforward, this approach presents limitations.

### 3.1 Surrogate quality assessment

A posteriori error estimators are employed to evaluate the residual error between the PCE prediction and the training set [15]. In particular, we employ the leave-one-out (LOO) mean square error estimator

$$\varepsilon_{LOO} = \frac{1}{n} \sum_{1=1}^{n} \Delta_i^2 \qquad \text{where} \quad \Delta_i = M(\boldsymbol{u}^{(i)}) - M_{PC \setminus i}(\boldsymbol{u}^{(i)}). \tag{6}$$

Here, $\Delta_i$ is the error between the CFD output and the PCE prediction at $\boldsymbol{u}^{(i)}$, obtained removing the $i$ point from the training set, see Ref. [15]. To evaluate the surrogate quality, we employ the $R^2$ score:

$$R^2 = 1 - \gamma \frac{\varepsilon_{LOO}}{\operatorname{Var}[\boldsymbol{y}]} \qquad \text{with} \quad \gamma = \frac{n}{n - \operatorname{card}(\mathcal{A})} \left(1 + \operatorname{tr}\left(\left(\boldsymbol{C}^T \boldsymbol{C}\right)^{-1}\right)\right), \tag{7}$$

where $\gamma$ is a correction factor for scarce training data sets [14]. $R^2 = 1.0$ is perfect predictive capability. $R^2 = 0.0$ implies the model does not explain data variability, but predicts the average.

### 3.2 Inference procedure

The following relationship between computational model $y$ and experimental observations $y^e$ is assumed

$$y^e(\boldsymbol{x}) = y(\boldsymbol{x}, \boldsymbol{u}) + e(\boldsymbol{x}) \qquad \text{with} \quad e(\boldsymbol{x}) \sim \mathcal{N}(0, v(\boldsymbol{x})), \tag{8}$$

where $\boldsymbol{x}$ is the spatial coordinate and $e(\boldsymbol{x})$ is a space-dependent measurement uncertainty (assumed statistically independent from the uncertain model parameters $\boldsymbol{u}$). Note that we neglect any model bias. Note also that experimental observations are available at a discrete locations $\{\boldsymbol{x}_i^e\}_{i=1}^{n_e}$, and can be represented by a vector $\boldsymbol{y}^e = \{y^e(\boldsymbol{x}_i^e)\}_{i=1}^{n_e}$.

The calibration problem is treated as a Bayesian inverse problem. Namely, we employ a modular maximum a posteriori (MAP) approach, following the statistical framework introduced in Ref. [16]:

1. We obtain an estimate of the measurement uncertainty $e(\boldsymbol{x})$ from the observed data $y^e(\boldsymbol{x})$.
2. We perform a MAP estimate of the uncertain inputs, given $e(\boldsymbol{x})$, the numerical data set $\{\mathcal{U}, \boldsymbol{y}\}$, and the experimental observations $\boldsymbol{y}^e$.

The modular approach avoids identifiability problems which can derive from a joint estimation of the measurement uncertainty and the uncertain inputs. Moreover, the measurement error should be estimated independently from the surrogate approach used to model the relationship between the numerical code and the uncertain inputs. In the following, the two calibration steps are discussed separately.

#### 3.2.1 Measurement uncertainty

Discontinuities inherent in the hypersonic flow field of interest render the measure uncertainty subject to spatially variable precision. We account for this in our approach to noise estimation from experimental data and resort to Heteroscedastic Gaussian Process (HGP) modeling following the variational formulation of Ref. [17]. In this framework, the observation is assumed to be the sum of an unknown true physical process $g(\boldsymbol{x})$ and the noise term $e(\boldsymbol{x})$:

$$y^e(\boldsymbol{x}) = g(\boldsymbol{x}) + e(\boldsymbol{x}) \qquad \text{where} \quad g(\boldsymbol{x}) \sim \mathcal{GP}(0, k_g(\boldsymbol{x}, \boldsymbol{x}')) \quad \text{and} \quad e(\boldsymbol{x}) \sim \mathcal{N}(0, r(\boldsymbol{x})), \tag{9}$$

meaning that a generic (unknown) function is modeled as a zero-mean Gaussian Process (GP) model with covariance function $k_g$, while the measurement noise is normally distributed with a space-dependent variance $r(\boldsymbol{x})$. The key idea idea behind HGP is to define $r(\boldsymbol{x}) = e^{h(\boldsymbol{x})}$, to ensure variance positivity, and assume $h(\boldsymbol{x}) \sim \mathcal{GP}(\mu_0, k_h(\boldsymbol{x}, \boldsymbol{x}'))$. The hyperparameters of the HGP model govern the covariance functions $k_g$, $k_h$, and $\mu_0$ and modulate the noise scale. The estimation of the hyperparameters is achieved by numerically optimizing the analytical lower bound of the log-posterior of the observations $\log p(\boldsymbol{y}^e)$. For further methodological aspects on GP, HGP, and variational approaches, refer to [18, 17, 19]. Once the HGP is correctly trained, we obtain an analytical estimate of the variance at the spatial location of the observations, namely $\boldsymbol{r} = \{r(\boldsymbol{x}_i^e)\}_{i=1}^{n_e}$.

#### 3.2.2 MAP estimate

The MAP approach is based on maximizing a loss function composed by the likelihood of the observations and the prior of the uncertain inputs. For numerical stability reasons, the sum of the logarithms is used instead of the product:

$$\boldsymbol{u}^\star = \underset{\boldsymbol{u} \in \Omega}{\operatorname{argmax}} \left[\mathcal{L}_{\text{like}}(\boldsymbol{u}) + \mathcal{L}_{\text{prior}}(\boldsymbol{u})\right]. \tag{10}$$

Since the surrogates are constructed using the numerical dataset $\{\mathcal{U}, \boldsymbol{y}\}$ independently at each grid point, the observation at a specific location $\boldsymbol{x}_i^e$ is calibrated independently.

The likelihood of the observation at each location is assumed to be normal

$$\mathcal{L}_{\text{like}}(\boldsymbol{u}) = -\frac{n_e}{2}\log(2\pi) - \frac{1}{2}\log\left(\prod_{i=1}^{n_e} r(\boldsymbol{x}_i^e)\right) - \frac{1}{2}\sum_{i=1}^{n_e}\frac{(y^e(\boldsymbol{x}_i^e) - M_{PC}(\boldsymbol{x}_i^e, \boldsymbol{u}))^2}{r(\boldsymbol{x}_i^e)}. \tag{11}$$

Instead, the prior has a simpler formulation due to the hypothesis of statistically independent inputs Eq. (2). Because of this, the prior term corresponds to the sum of the logarithm of the probability density function of each random input:

$$\mathcal{L}_{\text{prior}}(\boldsymbol{u}) = \sum_{i=1}^{d} \log p_{U_i}(u_i). \tag{12}$$

The loss function is optimized using a multi-start gradient-based method. Then, the calibrated input vector can be plugged into each surrogate to obtain the calibrated prediction. Also, it can be plugged into the numerical solver to verify the closeness of the numerical prediction to the observations.

## 4. Results

The UQ analysis targets QoIs evaluated at the wall of the double-cone, reported in Sec. 4.1, and over the whole computational domain, Sec. 4.2. The inference of the true inflow condition is in Sec. 4.3. Table 1 reports the alleged uncertainty modeled through a uniform probability distribution between the min/max values. In the table, $u_\infty$ is the axial velocity, $T_\infty$ is the gas roto-translational temperature, $p_\infty$ is the pressure, $Y_{O_2,\infty}$ is the $O_2$ mass fraction, and $\Delta T_\infty$ is a differential temperature used to model the thermal nonequilibrium at the inflow, with $\Delta T_\infty = T_{v,\infty} - T_\infty$ by definition. The reference experiment [3] has an inflow at thermal nonequilibrium with $T_{v,\infty} > T_\infty$, therefore $\Delta T_\infty > 0$.

| | $u_\infty$, m/s | $T_\infty$, K | $p_\infty$, Pa | $Y_{O_2,\infty}$, - | $\Delta T_\infty$, K |
|---|---|---|---|---|---|
| Upper Bound | 4000 | 1000 | 200 | 0.95 | 200 |
| Lower Bound | 3500 | 400 | 100 | 0.75 | 0 |

Table 1: Uncertainty bounds.

A set of $N = 120$ Monte Carlo realizations of the CFD model is considered. The random inflow conditions are sampled through Latin Hypercube. All PCE are truncated considering $r = 3$. For a 5-dimensional random input space, the cardinality card($\mathcal{A}$) of the polynomial basis is 56.

### 4.1 Wall QoIs

We consider QoIs extracted along the solid wall. First, we assess the quality of surrogates and later we present the UQ analysis reporting the Probability Density Function (PDF) and Sobol' indices. The PDF is obtained through a surrogate-based sample-wise kernel density estimation [14].

#### 4.1.1 Surrogate quality assessment

Figure 2 reports the LOO-based $R^2$ score over the solid wall for three QoIs. Namely, the static pressure $p$, the $O_2$ mass fraction $Y_{O_2}$, and the heat-flux $q$.

Overall, surrogates are of fair quality since $R^2 \geq 0.9$ is considered a high threshold. The $p$ and $Y_{O_2}$ surrogates show a quality indicator always close to unity, as desired, except for small regions corresponding to limited locations where shock waves are present. The same is detected for $q$, although the quality reduction around $x = 0.1$ is larger. We can identify two regions where quality departs significantly from unity ($x \approx 0.075$ and $x \approx 0.1$). These are where separated the regions develop or where shocks impinge. However, there the $R^2$ remains reasonable despite the highly nonlinear flow behavior.

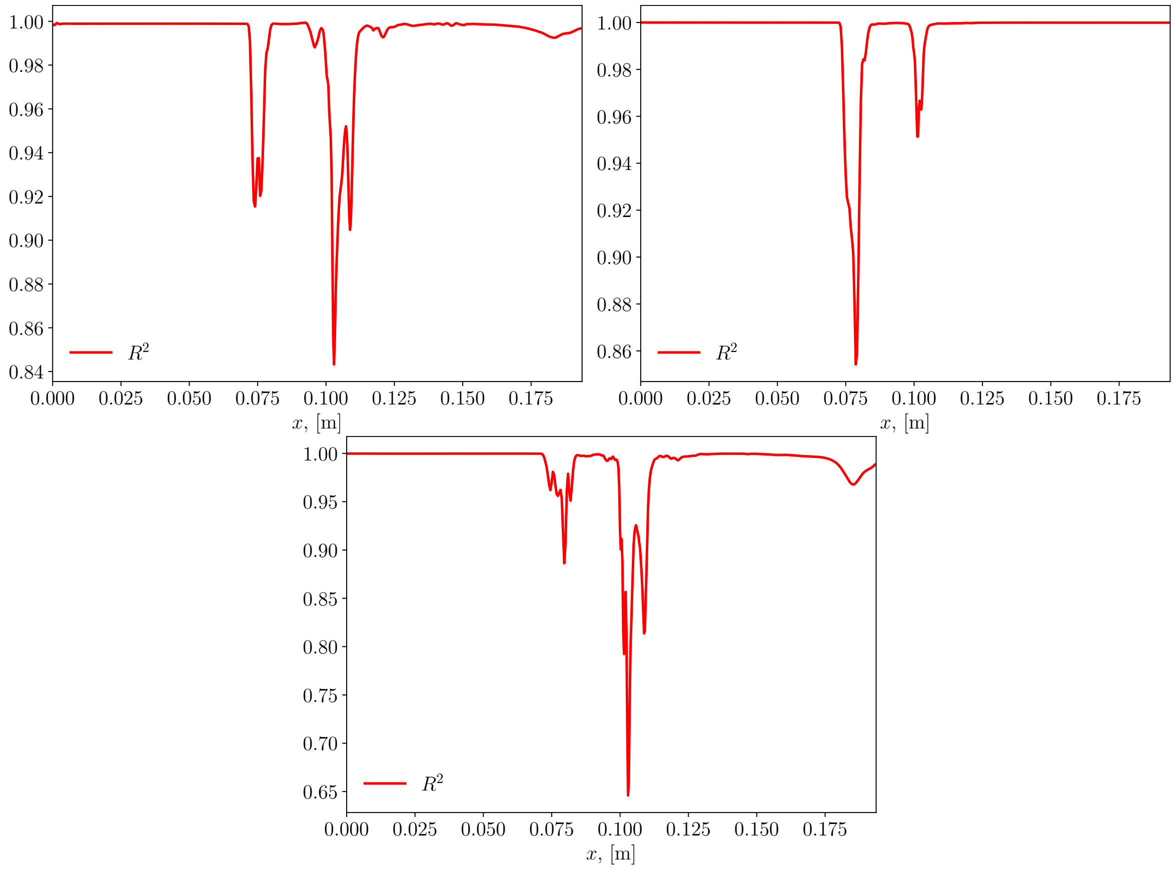


Figure 2: PC surrogate quality assessment, $p$ (upper left), $Y_{O_2}$ (upper right), and $q$ (lower center).

#### 4.1.2 UQ analysis

We report the PDF of the model outputs over the wall in Fig. 3. To help the visualization, PDFs are normalized by their peak value. The mean value is highlighted by the orange line. Starting from the pressure (upper left figure), we observe a very small variability in the region of the first cone. A sudden increase in uncertainty occurs in the separation region upstream of the second cone. Downstream, we observe the pressure peak due to the second shock and a following expansion where the largest uncertainty is detected. Moreover, the PDF is highly skewed as its peak is clearly distinct from the mean value. Then, the expansion after the second cone is associated with very low pressure values and low uncertainty. Moving to $Y_{O_2}$, we detect a large uniform uncertainty over the first cone, which is directly related to the variability of the inflow. This uncertainty is altered only marginally by the first shock, triggers little chemical dissociation. The shock interaction increases the $O_2$ mass fraction and reduces the uncertainty. The expansion along the second cone and downstream of it leads to a reduction of $Y_{O_2}$ and to an increase in uncertainty. In this region, the PDF appears to be bi-modal, with a clear darker region below $\mu$ and a small lighter peak above. Considering the heat-flux $q$, the uncertainty is lower than for $p$ and $Y_{O_2}$. A larger uncertainty is present in the shock interaction region ($x \approx 0.10$). However, this region corresponds to a low surrogate quality.

The global sensitivity analysis is performed through analysis of variance (ANOVA) and reported in Fig. 4. The variance decomposition highlights the first-order effect of the five uncertain inputs on the CFD model output. In each plot, regions where surrogates suffers from loss in quality, i.e., $R^2 < 0.9$, are blackened. The analysis of the static pressure reveals a primary role of the uncertainty affecting the freestream static pressure, as expected, and the freestream roto-translational temperature. This is true for both regions upstream and downstream the second shock. Around $x = 0.075$ and $x = 0.1$ we can see that the white region not covered by Sobol' indices has a larger extension compared to other locations. Here, high-order

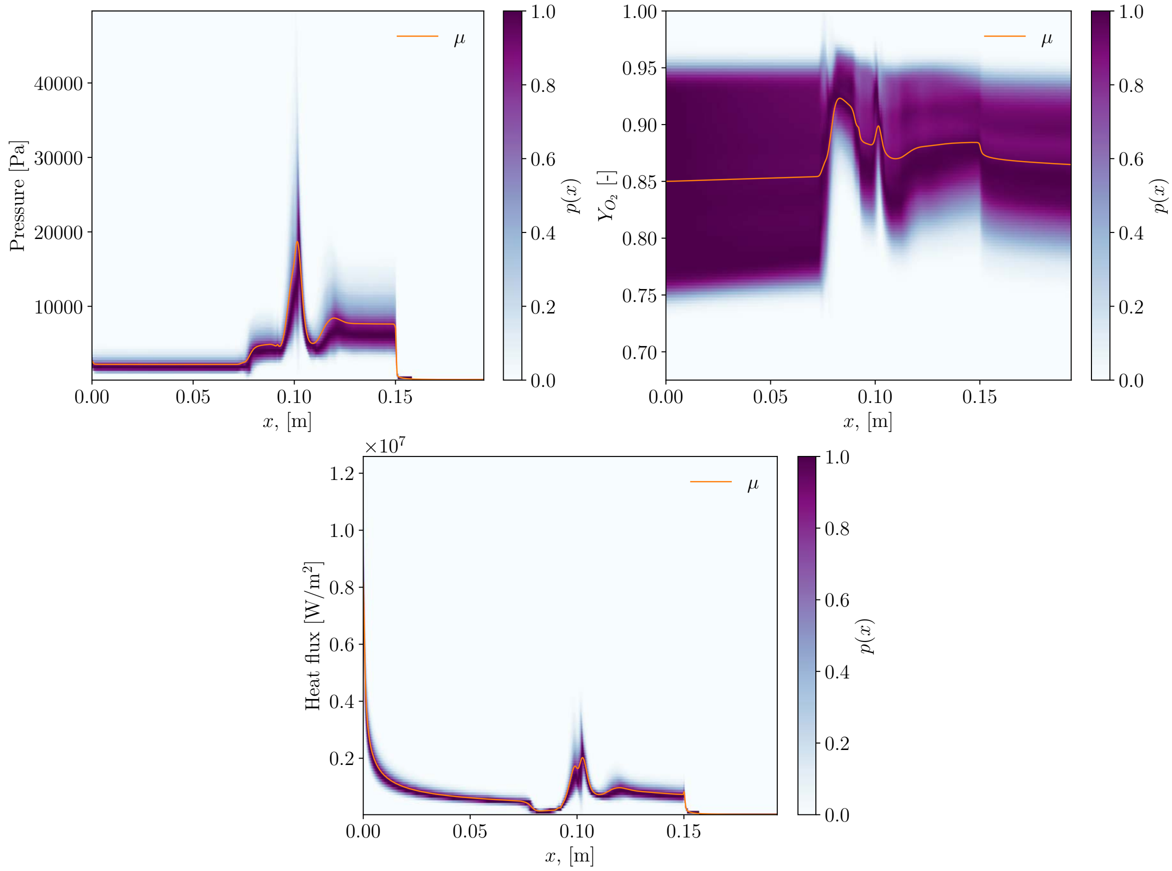


Figure 3: UQ analysis of QoIs along the solid wall, $p$ (upper left), $Y_{O_2}$ (upper right), and $q$ (lower center). Each plot reports the PDF (normalized by its peak value) and the mean value (orange line).

effects play a not negligible role. We observe a null effect of $\Delta T$ i.e., the parameter controlling the inflow nonequilibrium. Instead, the $O_2$ mass fraction is mostly affected by the inflow composition, especially in the first portion of the domain. After the second shock, $u$, $p$, and $T$ begin to exert limited influence, but nothing compared to $T$. Again, first-order effects associated with $\Delta T$ are negligible. Considering the heat-flux $q$, in the first cone region the largest variability is due to $u$, but a comparable role is played by $p$ and $T$. High-order effects are observed in the region between the shock interaction and the second shock. In the expansion region downstream the cone, we observe a very high influence of the inflow axial velocity and a contribution from $Y_{O_2}$.

Since a goal is to understand if the inflow nonequilibrium level has any effect on the wall QoIs, the total effect Sobol' indices of $\Delta T$ have been computed and reported in Fig. 5. Note that values are low and the $y$-axis scale is magnified. The influence of $\Delta T$ is similar for every QoI. A peak can be seen around $x \approx 0.075$, where the separation bubble is located. A lower but more extended peak is where shocks interact at $x \approx 0.1$. In the sole case of the heat-flux, inflow nonequilibrium impacts the variance close to the outlet, in the separation region downstream the double-cone geometry. Although these effects are very limited, they highlight the influence of the inflow nonequilibrium on $p$, $Y_{O_2}$, and $q$.

### 4.2 Field QoIs

The UQ analysis targets the Mach number $M$, the roto-translational temeprature $T$, and the vibro-electronic temperature $T_v$ fields. We first assess the PC surrogate quality over the domain. Then, we conduct an analysis limited to the regions where the surrogates are reliable.

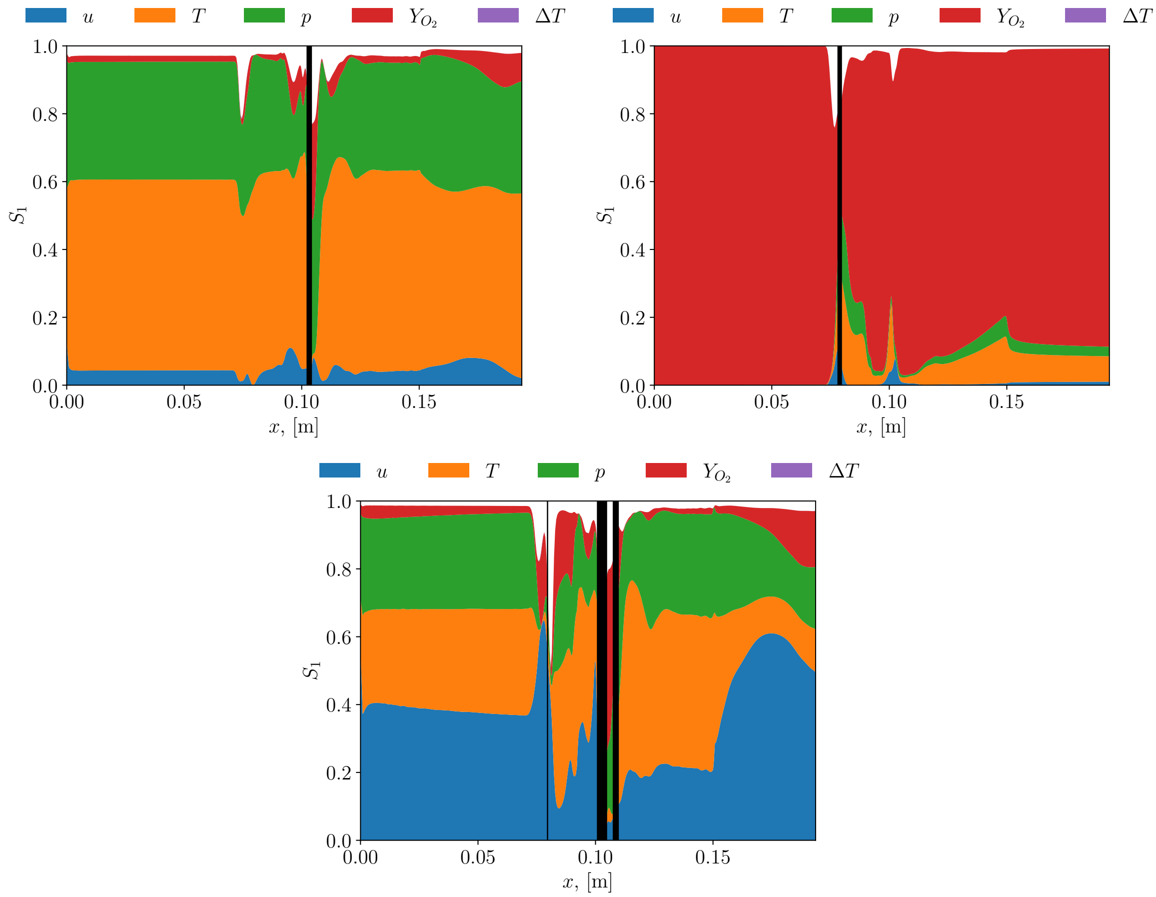


Figure 4: First order Sobol' indices of QoIs along the solid wall, $p$ (upper left), $Y_{O_2}$ (upper right), and $q$ (lower center). The black region corresponds to points where $R^2 < 0.9$.

### 4.2.1 Surrogate quality assessment

Figure 6 reports the LOO-based $R^2$ score for the three QoI fields. In all cases, the quality of surrogates is very high where the flow is smooth i.e., upstream and downstream shocks. Otherwise, quality reduces where shocks are present. In the forward region, low quality is found along the attached shock. This is explained by the fact that an uncertain inflow variates only slightly the shock angle. On the other hand, the region corresponding to the detached shock loses surrogates' quality dramatically. The $R^2$ behavior appears to be oscillating, signifying the appearance of the Gibbs phenomenon, strongly affecting the surrogate reliability.

### 4.2.2 UQ analysis

Global sensitivity analysis is performed on $M$, $T$, and $T_v$ fields, limited to regions where $R^2 > 0.9$ (Colorless regions appear to exclude poor surrogates). We report the Mach field analysis in Fig. 7. In the pre-shock region, the largest contribution to variance is due to the inflow roto-translational temperature. Instead, the contributions in the post-shock region are peculiar. Indeed, $u$ influences the Mach variability only in the post-shock region external to the boundary layer, with peaks in the expansion region close to the outlet. Differently, $T$ is responsible for the variability of the Mach field inside the boundary layer. $p$ and $Y_{O_2}$ play a minor but complementary role, where $p$ behaves similar to $T$, while $Y_{O_2}$ to $u$. We note that the peak influence of $Y_{O_2}$ is inside the separation bubble upstream of the second cone. Again, $\Delta T$ has a negligible influence on the Mach variability.

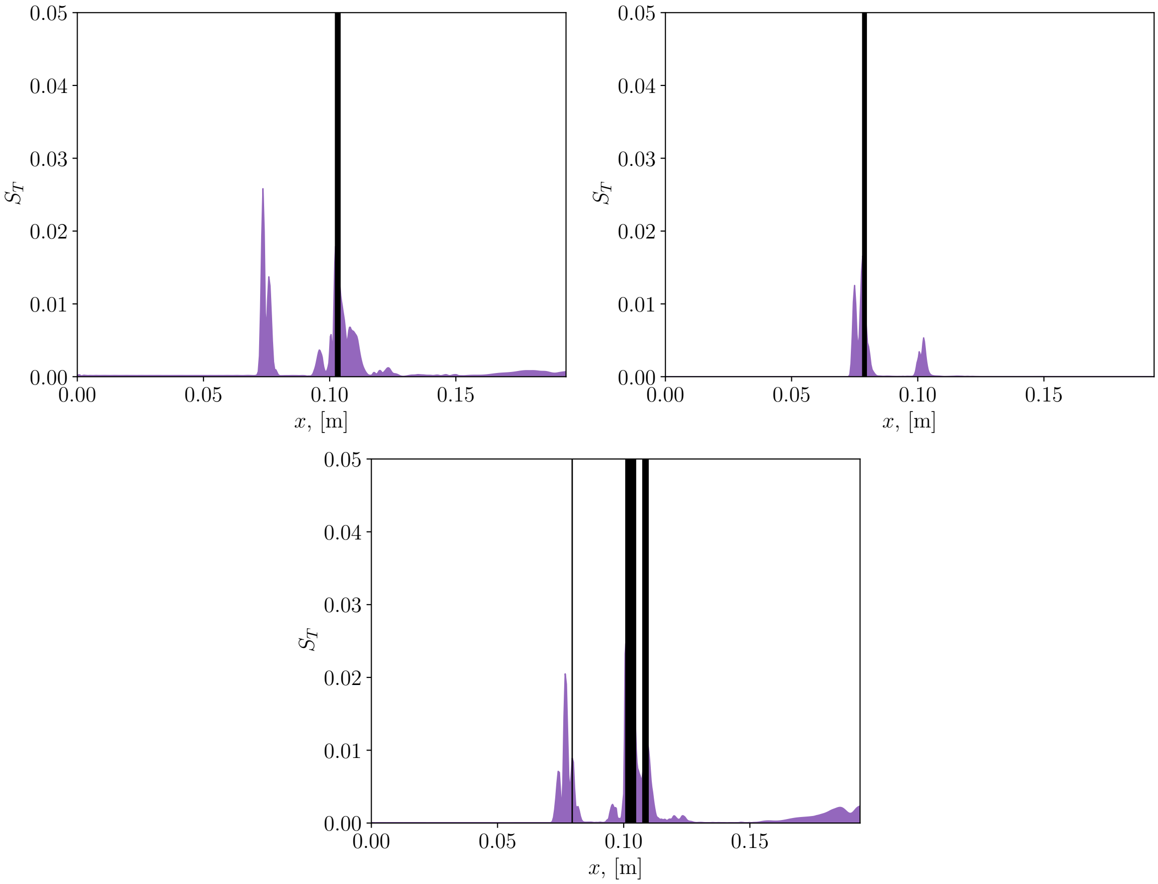


Figure 5: Total order Sobol' $\Delta T$ index of QoIs along the solid wall, $p$ (upper left), $Y_{O_2}$ (upper right), and $q$ (lower center). The black region corresponds to points where $R^2 < 0.9$.

The first-order Sobol' indices of the roto-translational temperature field are reported in Fig. 8. As for the Mach field, the inflow $T$ dominates the influence on the temperature in the pre-shock region. The most interesting region is the post-shock one, where $u$ highly influences the temperature over the whole extent of the boundary layer and in separated regions i.e., the bubble upstream the second cone and the near-outlet. First order effects due to $T$ are strong in the region downstream of the detached shock outside the boundary layer. In the same area, also the inflow static pressure is partially responsible for the uncertainty. The inflow $O_2$ mass fraction effect are more relevant in the near-outlet region. Qualitatively, similar results are found for the vibro-electronic temperature, with minor differences in the Sobol' indices field associated with the inflow $T$ and $Y_{O_2}$. Plots are not reported.

### 4.3 Calibration

The calibration of uncertain inflow condition w.r.t. experimental observations is performed following the approach of Sec. 3.2. The experimental data refer to Run-87 from Ref. [3] and consists of static pressure ($\boldsymbol{p}^e$) and the heat-flux ($\boldsymbol{q}^e$) measurements at the solid wall. Three calibration procedures have been performed. (i) Calib-1 considers $\boldsymbol{p}^e$ and $\boldsymbol{q}^e$ simultaneously; (ii) Calib-2 considers $\boldsymbol{p}^e$ only; (iii) Calib-3 considers $\boldsymbol{q}^e$ only.

Table 2 compares the experimental inflow conditions with the three calibrated conditions. Calib-1 returns a $u_\infty$ close to the experimental value and on the upper bound. The roto-translational temperature is instead significantly lower than the experiment, indicating that the framework is trying to justify the discrepancy between the predicted and the reference data with a different inflow temperature. Instead, Calib-2,3 infer a similar velocity value, but a higher roto-translational temperature. In particular, Calib-2

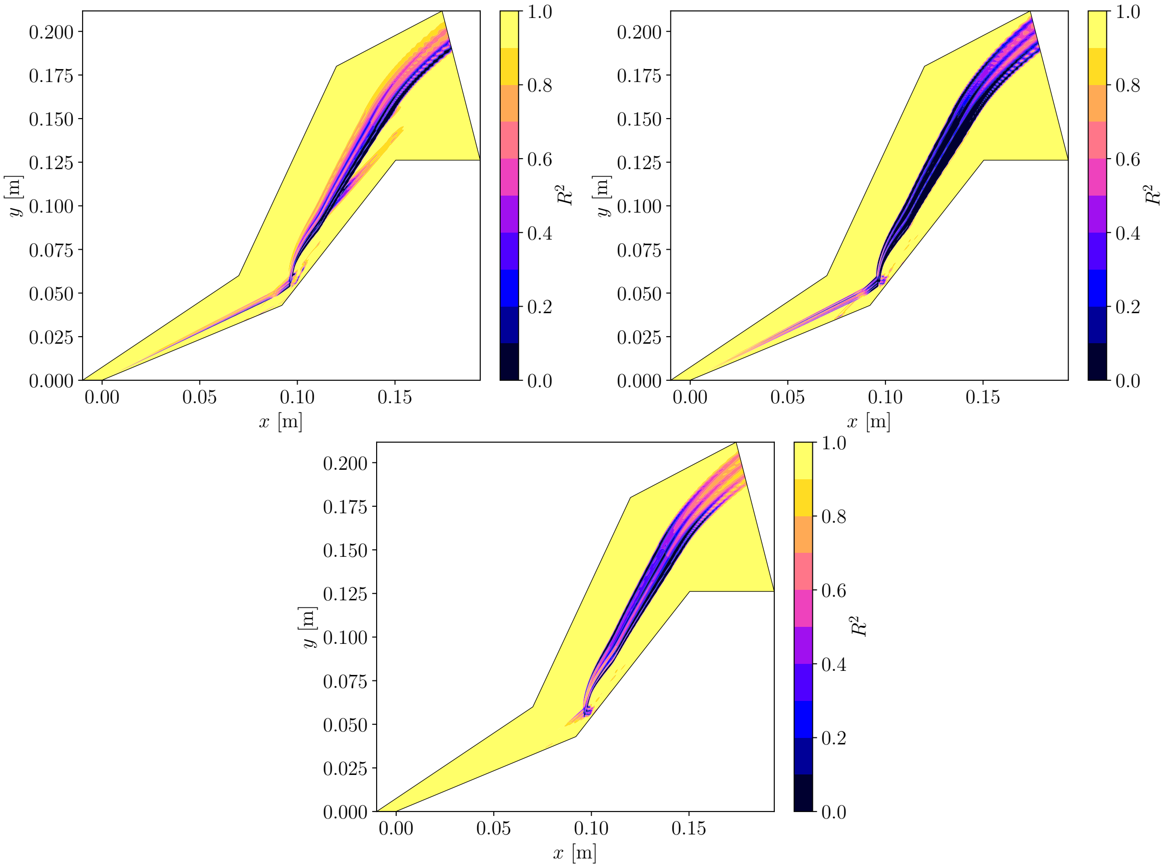


Figure 6: PC surrogate quality assessment, $M$ (upper left), $T$ (upper right), and $T_v$ (lower center).

has a temperature similar to the experiment, and justifies discrepancy with a different inflow velocity. All three calibration return a similar value of $p_\infty$ (200 Pa), which is the highest allowable within the uncertain bounds. The same (but opposite) occurs for the $O_2$ mass fraction which allegedly is the lowest possible (0.75). Note that both the inferred $p_\infty$ and $Y_{O_2}$ are inferred on the uncertainty bound and are different from the experiment. Considering the differential inflow temperature $\Delta T_\infty$ all three calibrations report a higher inflow thermal nonequilibrium compared to Run-87. In the following, the model predictions corresponding to the calibrated inflow conditions will be analyzed.

| | $u_\infty$, m/s | $T_\infty$, K | $p_\infty$, Pa | $Y_{O_2,\infty}$, - | $\Delta T_\infty$ ($T_{v,\infty}$), K |
|---|---|---|---|---|---|
| Run-87 [3] | 4019 | 625 | 165 | 0.9245 | 87 (712) |
| Calib-1 | 4000 | 401 | 200 | 0.75 | 115 (516) |
| Calib-2 | 3500 | 616 | 200 | 0.75 | 165 (781) |
| Calib-3 | 3568 | 526 | 200 | 0.75 | 138 (664) |

Table 2: Run-87 inflow conditions vs. differently calibrated inflow conditions.

The Calib-1 pressure and heat-flux profiles reported in Fig. 9. In both cases, we report the numerical realizations, the experimental observations, the surrogates prediction using the calibrated values (red line), and the CFD simulation using the calibrated values (blue line). Starting from the static pressure on the left, we observe that the calibrated profiles (both predicted and simulated) differentiates from the observations in some regions. In the experiments, the onset of the separation occurs before all the numerical samples. In the area around the shock interaction at $x \approx 0.1$, the calibrated profile reaches a peak lower than the majority of the numerical samples, and matches the qualitative trend of the observations quite well. In the first expansion region, observations appears to be noisy, making the calibration process difficult.

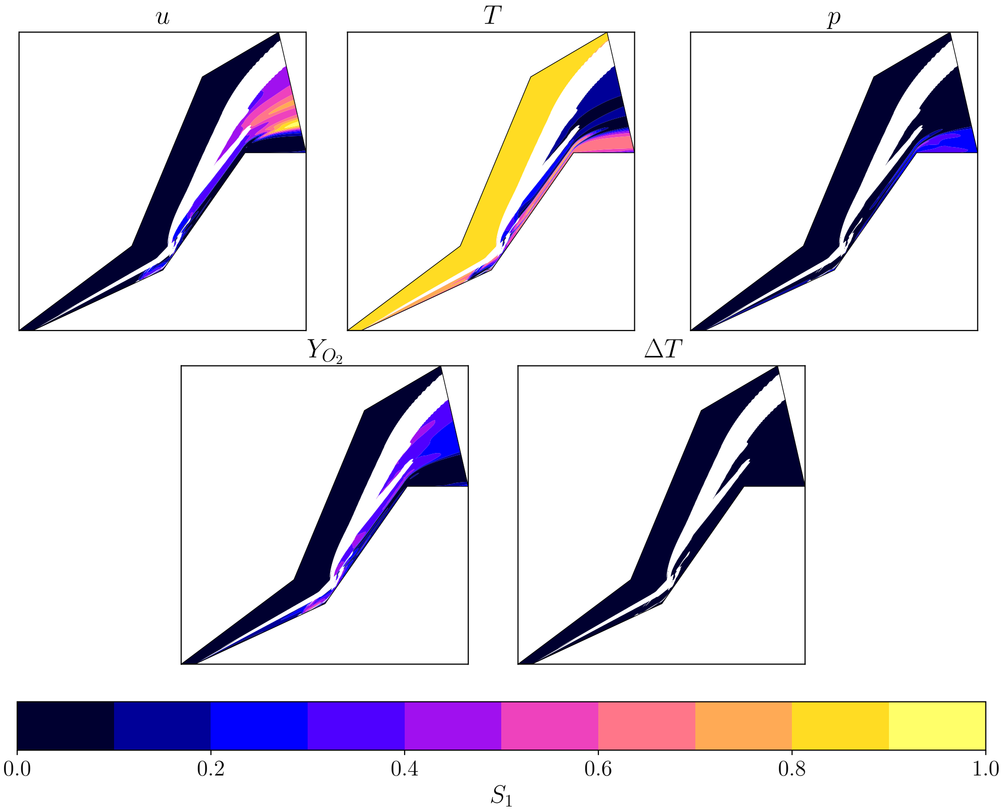


Figure 7: First order Sobol' indices of Mach field.

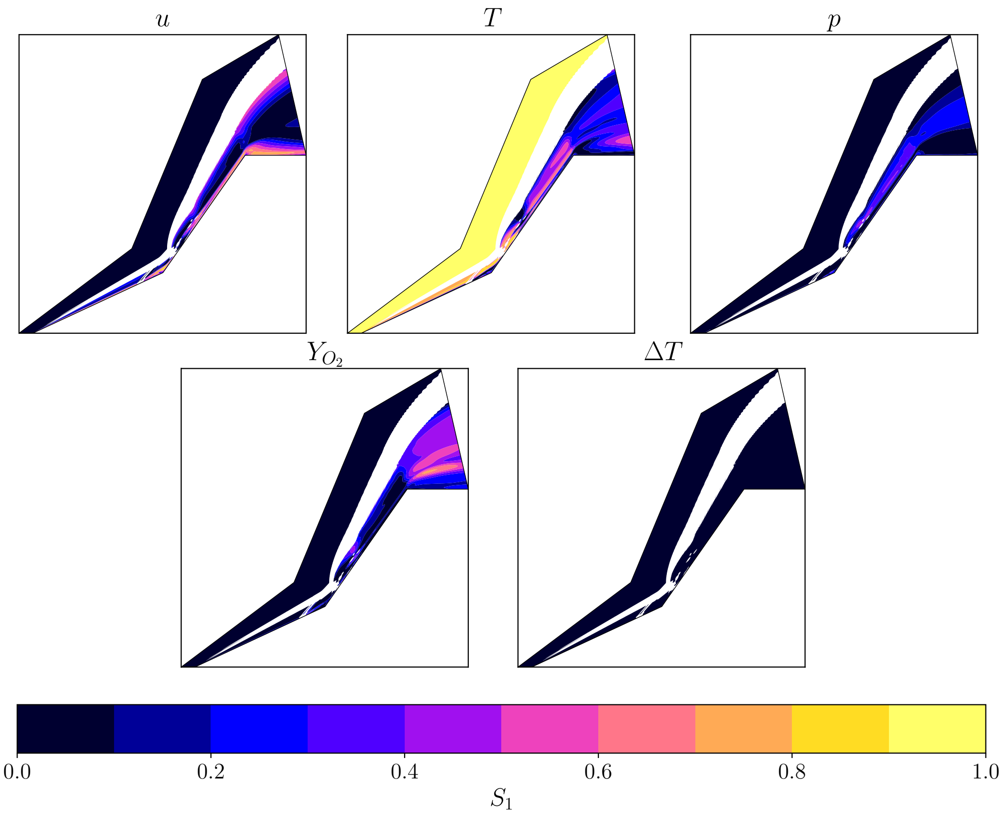


Figure 8: First order Sobol' indices of roto-translational temperature field.

Although the heat-flux trend is different, the differences between calibrated profiles and observations have the same explanation. The CFD model is not able to capture the onset of the circulation bubble. The calibration process attempts to capture the separation, deteriorating heat-flux predictions along the first cone. Also, the shock interaction is not qualitatively captured by the calibrated profiles, even though these are generally closer than the numerical samples. The first expansion region is, again, very noisy and is not perfectly captured by the calibrated profiles.

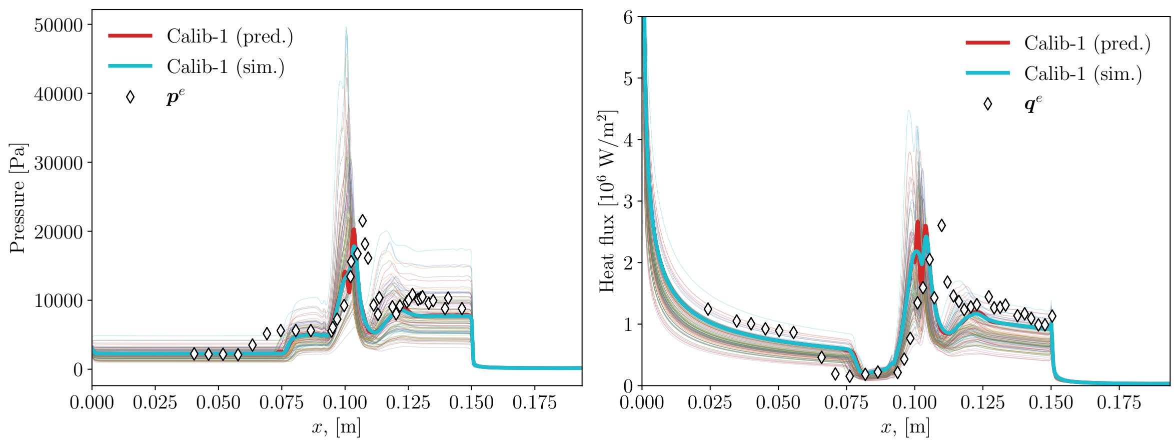


Figure 9: Calibrated prediction and simulation vs. experimental data. (Left) Calib-1 for pressure, (right) Calib-1 for heat-flux. Numerical samples are reported in the background.

The Calib-2 pressure and the Calib-3 heat-flux profiles are reported in Fig. 10. From a qualitative standpoint, in both cases associated with Calib-2 the surrogate-based predictions (red lines) show nonphysical behavior in the separation region around $x = 0.075$. This indicates that the inferred values lead to some irregularities between independent PCE predictions at different locations. Building a PCE capable of accounting for the spatial correlation may improve results.

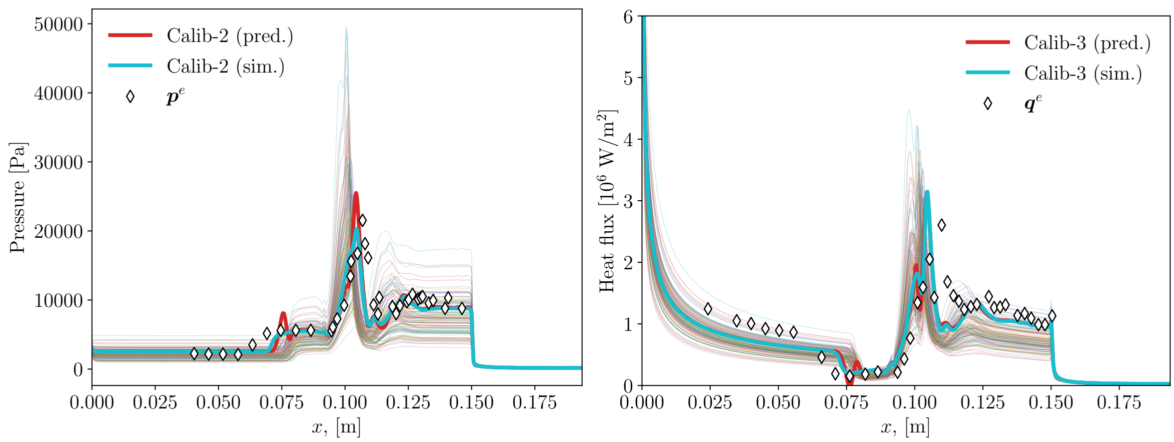


Figure 10: Calibrated prediction and simulation vs. experimental data. (Left) Calib-2 for pressure, (right) Calib-3 for heat-flux. Numerical samples are reported in the background.

## 5. Conclusions

We report a detailed UQ analysis of a reference experiment in hypersonics. The use case consists in a axisymmetric double-cone subject to a hypersonic stream at high thermochemical nonequilibrium. The test is approximated as 2D in a computerized model employed to generate numerical data to drive the UQ analysis. This latter targets the most relevant QoIs, including the flow compositions, and focuses on investigating the physics over the solid wall and inside the flow region surrounding the model. A Bayesian procedure is carried out to infer the true inflow conditions attained in the experiment, in the aim of providing a justification between predictions and observations. We find that the considered uncertainty fails in explaining such mismatch, suggesting that additional modeling assumptions should be questioned. A possible target could be the isothermal hypothesis formulated w.r.t. the double cone surface. Literature [20] shows that the wall temperature plays a major role in determining the flow development around the model, possibly governing the extent of the separated region over the first cone.

## Acknowledgements

This work is supported by the HERMES project funded by the European Union - Next Generation EU, MUR Progetti di Ricerca di Rilevante Interesse Nazionale (PRIN2022, project n. 2022YPMRNW, CUP D53D23004340001). The authors acknowledge the CINECA award under the ISCRA initiative, for the availability of high performance computing resources and support under the allocation HP10CLT5LS.

## References

[1] D. Ninni, F. Bonelli, G. Colonna, and G. Pascazio. On the influence of non equilibrium in the free stream conditions of high enthalpy oxygen flows around a double-cone. *Acta Astronautica*, 201:247–258, 2022.

[2] D. Ninni, F. Bonelli, G. Colonna, and G. Pascazio. Unsteady behavior and thermochemical non equilibrium effects in hypersonic double-wedge flows. *Acta Astronautica*, 191:178–192, 2022.

[3] I. Nompelis and G. Candler. Numerical investigation of double-cone flow experiments with high-enthalpy effects. In *48th AIAA Aerospace Sciences Meeting Including the New Horizons Forum and Aerospace Exposition*, page 1283, 2010.

[4] G. Pascazio, D. Ninni, F. Bonelli, and G. Colonna. Hypersonic flows with detailed state-to-state kinetics using a GPU cluster. In *Plasma Modeling (Second Edition): Methods and applications*. IOP Publishing, 2022.

[5] R.N. Gupta, J.M. Yos, R.A. Thompson, and K. Lee. A review of reaction rates and thermodynamic and transport properties for an 11-species air model for chemical and thermal nonequilibrium calculations to 30000 K. *NASA STI/Recon Technical Report N*, 90:27064, 1990.

[6] G.S.R. Sarma. Physico–chemical modelling in hypersonic flow simulation. *Progress in Aerospace Sciences*, 36(3-4):281–349, 2000.

[7] R.B. Bird, W.E. Stewart, and E.N. Lightfoot. *Transport Phenomena revised 2nd Edition*. John Wiley & Sons, Inc New York, 2006.

[8] E.A. Mason and S.C. Saxena. Approximate formula for the thermal conductivity of gas mixtures. *The Physics of fluids*, 1(5):361–369, 1958.

[9] C. Park. Review of chemical-kinetic problems of future NASA missions. I-Earth entries. *Journal of Thermophysics and Heat transfer*, 7(3):385–398, 1993.

[10] J.L. Steger and R.F. Warming. Flux vector splitting of the inviscid gasdynamic equations with application to finite-difference methods. *Journal of computational physics*, 40(2):263–293, 1981.

[11] G. Jiang and C. Shu. Efficient implementation of weighted ENO schemes. *Journal of computational physics*, 126(1):202–228, 1996.

[12] O. Le Maître and O. Knio. *Spectral Methods for Uncertainty Quantification*. Scientific Computation. Springer Netherlands, 1 edition, 2010.

[13] D. Xiu. *Numerical methods for stochastic computations: a spectral method approach*. Princeton university press, 2010.

[14] B. Sudret. Polynomial chaos expansions and stochastic finite element methods. *Risk and reliability in geotechnical engineering*, pages 265–300, 2014.

[15] G. Blatman. *Adaptive sparse polynomial chaos expansions for uncertainty propagation and sensitivity analysis*. PhD thesis, Universite Blaise Pascal-Clermont II, 2009.

[16] P. Arendt, D. Apley, and W. Chen. Quantification of model uncertainty: Calibration, model discrepancy, and identifiability. *Journal of Mechanical Design*, 134:100908, 09 2012.

[17] M. Lázaro-Gredilla and M.K. Titsias. Variational heteroscedastic gaussian process regression. In *ICML*, pages 841–848, 2011.

[18] C.K.I. Williams and C.E. Rasmussen. *Gaussian processes for machine learning*, volume 2. MIT press Cambridge, MA, 2006.

[19] M.K. Titsias. Variational learning of inducing variables in sparse gaussian processes. In *Artificial intelligence and statistics*, pages 567–574. PMLR, 2009.

[20] V Viti, K Zore, A Jain, S Gao, JS Cagnone, J Stokes, and L Zori. Thermal non-equilibrium and conjugate heat transfer effects: Numerical validation for four hypersonic cases. In *AIAA Aviat. Aeronaut. Forum Expo. AIAA Aviat. Forum*, 2021.